Effects of rare earth element Gd on microstructure, thermodynamic parameters, mechanical, and shape recovery properties of CuAlTa alloys

Ercan Ercan[1] · Emre Bahadır Al[2] · Fethi Dağdelen[3]

Abstract

The microstructure, thermodynamic parameters, mechanical properties, and shape recovery properties of alloys consisting of $Cu_{83.5-x}Al_{13.5}Ta_3Gd_x$ ($x = 0, 0.5, 1$ mass%) alloy were investigated. Results showed that the addition of Gd to the alloys affects the martensite phase structure, creating new phases resembling snow crystals. An increase in Gd led to the formation of Al_3GdCu intermetallic phase structures. Furthermore, the study found that while Gd influenced the thermodynamic parameters, it did not impact the high-temperature shape memory feature. Through microstructure analysis, it was determined that the addition of Gd to the alloy resulted in thinning of the martensite and austenite phase structures, leading to a reduction in grain size and changes in crystallite size. The higher microhardness observed in the EE1 alloy was attributed to its denser β-Ta phase structures compared to other alloys.

Keywords Rare earth elements · Shape recovery properties · Martensite phase · Microstructure

Introduction

Shape memory alloys (SMAs) are a class of functional materials that can change their shape in response to temperature, stress, or magnetic fields [1–3]. Their unique feature lies in the transformation between the austenite and martensite phases in response to heating or cooling [4, 5]. SMAs exhibit three types of shape recovery: the one-way shape memory effect, the two-way shape memory effect, and superelasticity [6]. The temperature is the most significant factor influencing these features, which makes SMAs widely utilized in thermal applications, particularly for thermoelastic transformations [7, 8]. The two-way shape memory effect, which involves the formation of the austenite phase through heating of twinned martensite and the formation of twinned martensite through cooling of the austenite phase, serves as the fundamental working principle in thermal applications [3, 9]. The phase transformation temperatures in SMAs can vary depending on the composition [10] and the homogenization temperatures [11]. It is essential to determine the austenite start (A_s), austenite finish (A_f), martensite start (M_s) and martensite finish (M_f) temperatures, which represent the phase transformation temperatures, to evaluate the suitability of the alloy for a particular application [12].

Recently, there has been a growing popularity in manufacturing technology components such as microcontrollers, sensors, and actuators made from shape memory alloys, which are required to operate or shut down within a specific temperature range [2, 7, 13]. These components necessitate the use of SMAs with phase transformation capabilities, especially in high-temperature applications above 100 °C. Such applications are found in industries like aerospace, car engines, and electric motors [14]. As a result, there has been a strong emphasis on the development of high-temperature shape memory alloys (HTSMAs). This focus has led to extensive research and production of HTSMAs based on titanium, nickel, and copper [7, 15–17]. However, studies have indicated that Ti-based HTSMAs (such as Ti-Ni-Pd, Ti-Ta, etc.) and Ni-based HTSMAs (such as Ni–Mn–Ga, etc.) exhibit high costs,

✉ Ercan Ercan
eercan@beu.edu.tr

1 Department of Physics, Faculty of Science, Bitlis Eren University, 13000 Bitlis, Turkey

2 Department of Physics, Faculty of Science, Sivas Cumhuriyet University, 58140 Sivas, Turkey

3 Department of Physics, Faculty of Science, Firat University, 23200 Elazig, Turkey

poor processability, and low electrical conductivity. As a result, there has been a growing emphasis on the development of Cu-based HTSMAs [6, 18–21]. This is because Cu-based HTSMAs possess advantages such as low costs, easy processability, good conductivity, and high temperature transformation capabilities [22, 23]. Among Cu—based HTSMAs, SMAs such as Cu-Al-Ni, Cu-Al-Zn, and Cu-Al-Mn have garnered significant attention [24–26]. However, there is a need for further improvement and development in terms of phase transformation temperatures, microstructure characteristics, processability, shape memory effect (SME), superelasticity, and shape memory behaviors. This is driven by the increasing demand from engineering applications [22, 23].

Recently, the addition of Ta and Nb elements to CuAl—based alloys has resulted in the production of Cu-Al-Ta and Cu-Al-Ta-Nb SMAs [7, 13]. It has been discovered that these additions have formed a new group of HTSMAs with transformation temperatures above 200 °C [13].

The aim of this study is to produce new alloys by incorporating Gd, a rare earth element, and varying the chemical concentration of Cu, Al, and Ta elements. Alloys with different Gd proportions were successfully synthesized. The microstructure characteristics were analyzed using an optical microscope (OM), X-ray diffraction (XRD), and scanning electron microscope (SEM). XRD is employed to analyze the microhardness and phase characteristics of the samples. Energy-dispersive X-ray spectroscopy (EDX) is utilized to determine the chemical composition of the phase structures.

Differential scanning calorimeter (DSC) is employed to analyze the thermodynamic behavior of the alloys. Additionally, bend testing is conducted to evaluate the shape recovery rate (SRR).

Experimental

The production of new alloys involved the precise mixing of Cu, Al, Ta, and Gd elements in specified mass and atomic ratios, as outlined in Table 1. The production process was conducted in three stages. Firstly, the powder elements (Cu: 99.99%, Al: 99.99%, Ta: 99.9%, and Gd: 99.5% purity) were homogenized by thorough mixing with a mechanical mixer. Subsequently, the mixture was compressed into pellets using a mechanical press, applying an average pressure of 8 MPa. Finally, the alloys were generated by multiple melting cycles in an argon-controlled arc-melting system, followed by a homogenization process to establish the martensite phase structure. The alloys were subjected to a heat treatment by heating them to 850 °C for a duration of 24 h in an argon-controlled oven. Following this, the alloys were rapidly cooled by immersion in ice water containing a salt solution. Samples were sectioned/cut to facilitate the analysis of the microstructure, chemical composition, thermodynamic behavior, and shape memory behavior.

The sample sizes and corresponding analysis methods are provided in Table 2. Thermal analysis was performed using the Perkin Elmer Sapphire DSC device. For surface

Table 1 Compositional rate, electron concentration per atom, SRR and grain size of alloys

Alloys	Compositional rate in mass%				Compositional rate in at.%				e_v/a	SRR/%	Crystallite size/nm
	Cu	Al	Ta	Gd	Cu	Al	Ta	Gd			
EE0	83.5	13.5	3	–	72.74	26.22	1.04	–	1,561	56.14	32.02
EE1	83	13.5	3	0.5	72.47	26.29	1.04	0.2	1,571	56.66	51.64
EE2	82.5	13.5	3	1	72.20	26.36	1.04	0.4	1,576	58.46	39.86

Table 2 Analyzes, sample sizes and analysis method applied to alloys

Analyzes	Sample size	Analysis method
DSC	~60 (mg)	20 °C min^{-1}. and in the range of 90–450 °C, in N$_2$ medium
Optical microscope	~0.5 mm × 0.7 mm × 0.2 mm	Room temperature (50 μm and 25 μm magnification)
SEM	~0.5 mm × 0.7 mm × 0.2 mm	Room temperature, Vacuum medium (10 μm magnification)
EDX	~0.5 mm × 0.7 mm × 0.2 mm	Room temperature, Vacuum medium, Secondary electron
XRD	~0.5 mm × 0.7 mm × 0.2 mm	Room temperature, 2° min^{-1}. Scanning speed $(2\theta = 20 - 90°)$ (Cu$K_\alpha \lambda = 1,5418$)
Microhardness	~0.5 mm × 0.7 mm × 0.2 mm	Room temperature (0.3 HV)
SRR	~20 mm × 1.7 mm × 0.4 mm	Above A_f (450 °C)

morphology analysis, the samples underwent a preparation process involving sanding and polishing using DiaDoble Mono 1 μm diamond paste (with an Aka-Moran-U cloth) and Fumed Silica 0.2 μm diamond paste (with an Aka-Chemal cloth). The microstructures of the polished samples were visualized by subjecting them to chemical etching using a solution composed of FeCl36H2O (1.871 g), HCl (7.485 mL), and methanol (35.928 mL). Microstructure analysis was conducted using a Nikon MA/200 optical microscope, JEOL JSM 6510 SEM–EDX, RIGAKU ULTIMA IV XRD, and Mitutoyo microhardness devices. For the shape recovery rate (SRR) analysis, samples of the sizes specified in Table 2 were prepared accordingly. The bend testing samples were subjected to a heat treatment process by heating them in an oven at 900 °C for 2 min. Subsequently, they were cooled in salt-ice water to restore the martensite phase state, which may have been altered during the cutting and sanding procedures. The maximum deformation strain ratio (ε) is determined using the formula $\varepsilon = \frac{t}{t+D} \times 100\%$, where t represents the thickness of the strip sample and D denotes the diameter of the mold. In this study, the maximum deformation strain ratio was calculated to be approximately 21.42% for all the bending specimens. The alloys were subjected to deformation by an angle of θ_1 around a 1.1 mm mold. Subsequently, they were placed in an oven at approximately 450 °C above the A_f for a duration of 5 min. The shape recovery rate of the bend test samples was determined using the formula $n = \frac{\theta_1 - \theta_2}{\theta_1} \times 100\%$ where θ_2 represents the angle measured after the deformation.

Fig. 1 XRD patterns of alloys

Results and discussions

Cu-based alloys play a critical role in the formation of a metastable β martensite phase through a specific process involving high-temperature annealing followed by rapid cooling [27]. The process of high-temperature annealing followed by rapid cooling can induce changes in the phase structures of Cu-based alloys. Moreover, the introduction of additional elements and variations in the elemental ratios can further influence the phase structures of these alloys [7]. Research conducted on CuAlTa and CuAlTaNb alloys has provided valuable insights into the relationship between changes in elemental ratios and the resulting phase structures [13]. The objective of this study was to examine the influence of adjusting the elemental ratios in CuAlTa alloys and incorporating Gd elements on the resulting phase structures. Figure 1 illustrates the XRD patterns of both ternary CuAlTa and quaternary CuAlTaGd alloys at room temperature. The identification of phase peaks in the XRD patterns was based on existing literature research [7, 13, 28, 29]. Upon microstructural analysis of the alloys, it was observed
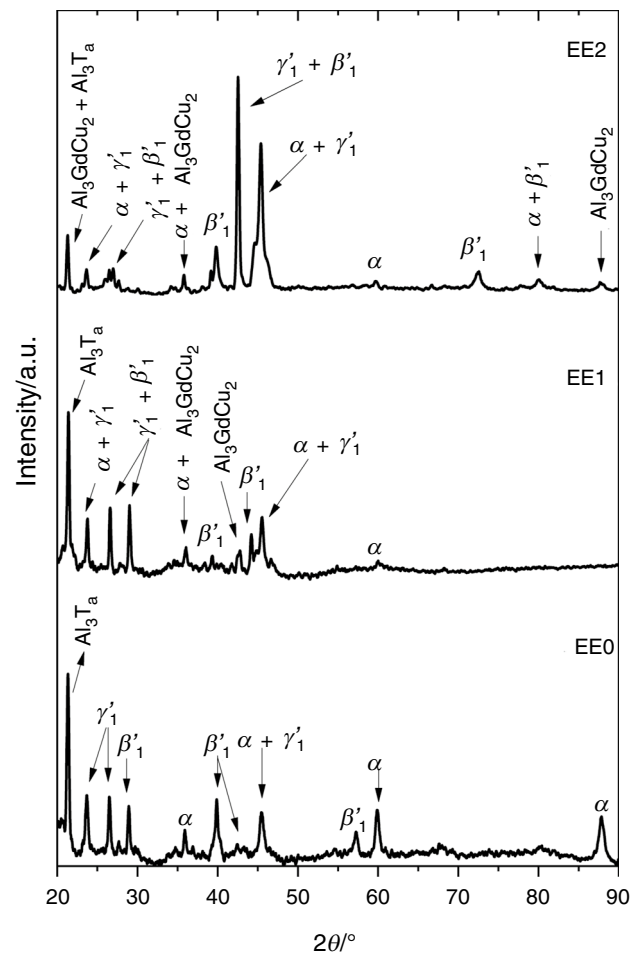
that the dominant phase peaks were martensite β_1' (18R) and austenite γ_1' (2H) phases. The analysis revealed that the dominant phase peaks were the martensite β_1' (18R) and austenite γ_1' (2H) phases. In the EE0 alloy, the intermetallic Al$_3$Ta (DO19) phase was also found as a single phase. Additionally, the addition of the Gd element to the EE1 and EE2 alloys resulted in the formation of intermetallic Al$_3$GdCu$_2$ phase peaks. It was also evident that all alloys exhibited the presence of the eutectoid $\alpha + \gamma_1'$ phase, resulting from the decomposition reaction of the β_1' martensite phase. In the rapid cooling process of the dominant β_1' martensite phase, it is important to ensure that the $\beta_1' + \gamma_1'$ transformation phase peaks are preserved even during order transitions [30]. The presence of phase peaks in the EE1 and EE2 alloys, resulting from the addition of Gd, indicates that Gd influences the transition of martensite phase peaks. This influence leads to the formation of $\beta_1' + \gamma_1'$ phase peaks. The inclusion of Gd as an additive is believed to play a role in various transformations occurring in the alloys, such as $\gamma_1' \rightarrow \alpha + \gamma_1'$, $\beta_1' \rightarrow \beta_1' + \gamma_1'$ and Al$_3$Ta $\rightarrow$ Al$_3$Ta + Al$_3$GdCu$_2$. The formation of α(Cu) precipitate [31] phase in conjunction with

Fig. 2 Optical microscope images of alloys
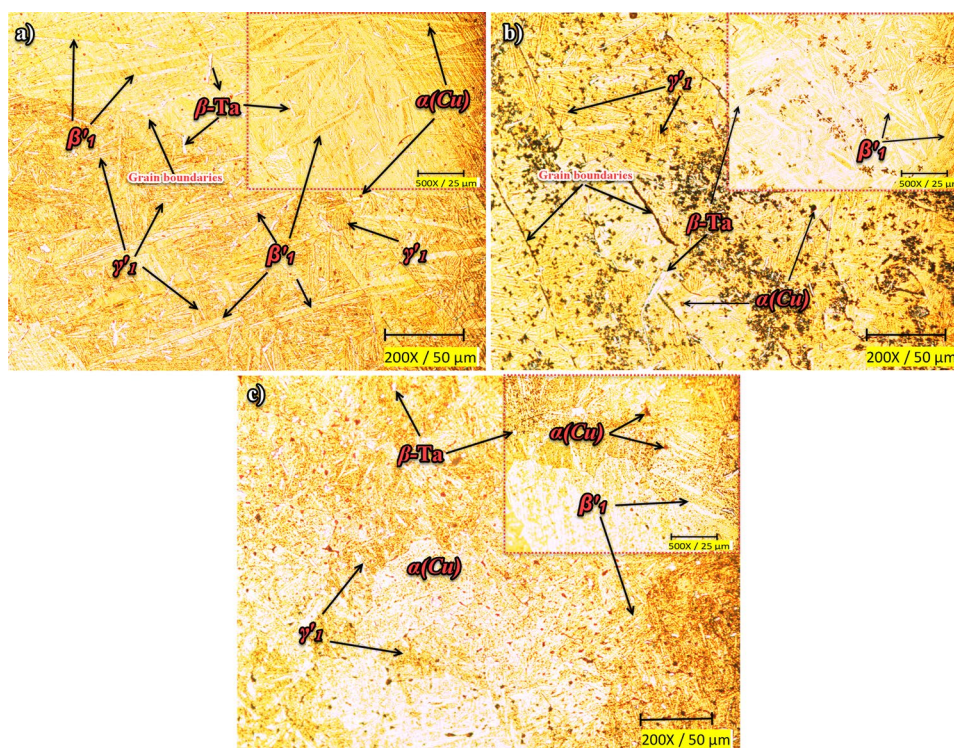
Al_3GdCu_2 intermetallic phase contributes to the formation of the $\alpha(Cu) + Al_3GdCu_2$ phase structures. The phase structures of martensite (β_1') and austenite (γ_1') in sample EE2 are tightly intertwined at 40–50° and form a sharp $\beta_1' + \gamma_1'$ phase structure. The β_1' martensite phase was found to be 57.32° in the EE0 alloy but disappeared in the EE1 alloy. In the EE2 alloy, the position of the peak shifted to 72.52°, resulting in the formation of β_1' martensite phase. Finally, the $\alpha(Cu)$ precipitate phase found at 87.86° in the EE0 was replaced by the Al_3GdCu_2 intermetallic compound.

The surface morphologies of the EE0, EE1, and EE2 alloys were examined using OM images (Fig. 2a–c). The OM images clearly reveal the presence of martensite (β_1') and austenite (γ_1') phases [7]. The phases can be distinguished in Fig. 2a–c by the difference in contrast, with the martensite phase structures appearing darker compared to the austenite phase structures. Based on the OM images, it was observed that in the EE0 alloy, the grain sizes formed by the existing phases were above 50 μm. However, with the addition of Gd, the grain sizes decreased below 50 μm. This suggests that the presence of Gd influences the grain size of the alloy, leading to a finer martensite (β_1') and austenite (γ_1') phase plates. Although the β-Ta and $\alpha(Cu)$ phases showed increased nucleation with the addition of Gd, their presence did not have a significant impact on the grain sizes.

Furthermore, in Fig. 2b, it can be observed that the β-Ta and $\alpha(Cu)$ phases are located within the grain boundaries and martensite phase structures. Particularly, the $\alpha(Cu)$ phases exhibit progression along the borders.

The SEM images in Fig. 3 provide valuable information about the surface structures of the alloys. The presence of martensite phase structures can be clearly observed in all alloys. These structures exhibit distinct features such as thin needle-like β_1' (18R) and the thick plate-like γ_1' (2H) structures [7]. The SEM micrographs reveal that with the addition of Gd, the thin needle-like β_1' and thick plate-like γ_1' phase structures are intertwined. The β_1' (18R) phase structures appear as thinner ridges compared to the γ_1' (2H) phase structure. This observation is in line with the results obtained from the XRD analyses, confirming the presence of these phase structures in the alloys. In the EE0 alloy, the β_1' phase is determined at four different peak points (~28.94°, 39.9°, 42.5°, 57.32°), while in the EE1 and EE2 alloys, it is determined at two points, ~39.38°, 44.14° and 39.88°, 72.52°, respectively. The γ_1' phase structure is identified at two different peak points, ~23.68° and 26.52°, in the EE0 alloy. However, it occurs as $\beta_1' + \gamma_1'$ at ~26.68°, 29.04° and ~26.96°, 42.5° in the EE1 and EE2 alloys, respectively. The EDX analysis reveals that the bright structures labeled as number 1 in all alloy samples correspond to the β-Ta phases (Fig. 3d–f). In particular, the EE1 and EE2 alloys exhibit β-Ta phases in rod-shaped forms. The EDX analysis also indicates that the higher content of Ta in the EE1 alloy compared to the other alloys leads to the formation of longer β-Ta structures in the EE1 alloy. The EDX analysis further reveals that in addition to the rod-shaped β-Ta phase structures in the EE2 alloy, there are bright point-like β-Ta structures that become more prominent and occupy other
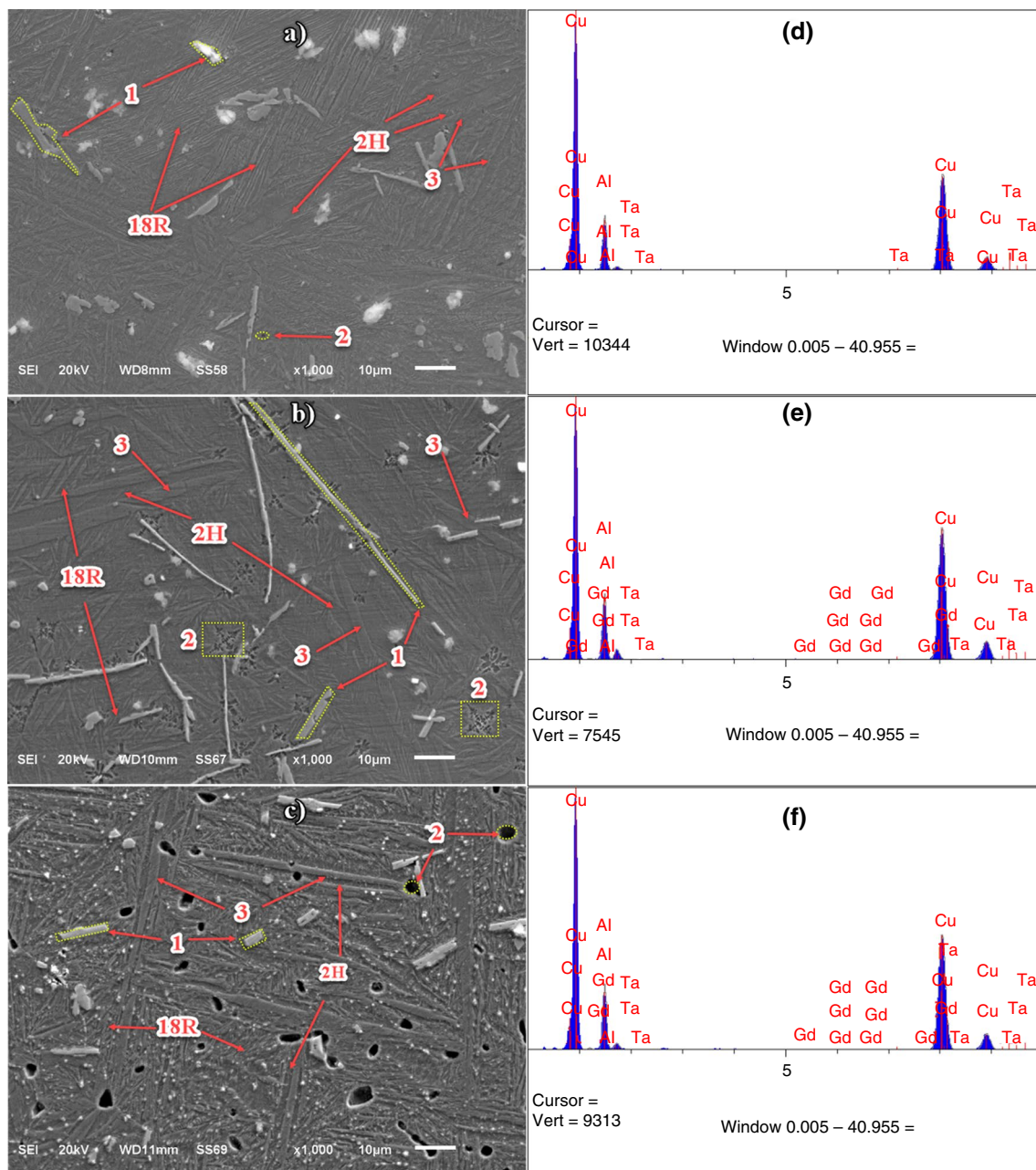
Fig. 3 SEM–EDX images of the alloys EE0 (**a–d**), EE1 (**b–e**) and EE2 (**c–f**)

phase structures. These bright point structures may indicate localized concentration of the β-Ta phase. Furthermore, the dark structures observed within the martensite plates, labeled as number 2 in the EE0 and EE2 alloys, are identified as α(Cu) precipitate phase structures. The EDX analysis indicates that the ratio of Cu in the α(Cu) precipitate phase structures, formed due to the rapid cooling of the alloy under high temperature conditions, is higher in the EE2 alloy. The addition of Gd rare earth element to the alloys leads to the formation of micro-voids within the α(Cu) precipitate phase structures. These micro-voids can be attributed to the

interaction between Gd and other alloying elements, which can induce lattice distortion and create voids during the phase transformation process. On the other hand, it is obvious that structures similar to the snow crystal structure in micron size are formed in the EE1 alloy. The XRD and EDX analyses indicate that the structures marked with number 3 in the alloys increase with the addition of Gd and correspond to the $\alpha + \gamma_1'$ phase structure. The increased Gd ratio in the EE2 alloy results in a clearer $\alpha + \gamma_1'$ phase structure. The grain sizes of α(Cu), β-Ta and $\alpha + \gamma_1'$ phase structures were determined to be below the order of 10 μm by SEM images.

Table 3 presents the elemental concentration values obtained from the EDX analysis of all phase structures identified in the alloys.

The presence of the metastable β phase in Cu-based alloys is significant for martensite transformations. Compared to other alloy groups, the β phase in Cu-based alloys is more intricate and can consist of multiple distinct phases coexisting [32]. Figure 4 presents the DSC analysis curves, which are utilized to determine the phase transformation temperatures in the alloys. The software of the DSC device is used to determine the transformation temperatures. Thanks to the software; The start/end point of the exothermic/endothermic change on the heat flow curves is determined. Then tangents are obtained from this point along the vertex and intersect with another tangent drawn along the temperature curve. The temperature value at this intersection point is determined as the transformation temperatures of the material. The DSC curves indicate that the $\gamma_1' \rightarrow \beta_1'$ and $\beta_1' \rightarrow \beta_1' + \gamma_1'$ martensitic phase transformations occur during heating and cooling, respectively [7, 33]. The shape memory characteristics of the alloys have been identified through these transformations, confirming their classification as shape memory alloys (SMAs) with transformation temperatures above 100 °C (Table 2), placing them in the category of high-temperature shape memory alloys (HTSMAs). The XRD patterns of the EE0 alloy exhibit single phases of β_1' and γ_1' which align with the minor peaks observed in the DSC analysis, indicating the formation of small peaks associated with the martensite transformation. The gradual broadening of the martensite transformation peaks in the EE2 alloy can be explained by the formation of β_1' and γ_1' phase peaks in the XRD patterns as $\beta_1' + \gamma_1'$. Additionally, being $\beta_1' + \gamma_1'$ requires more heat energy for martensitic transformations to occur during heating and cooling. By comparing the temperature values
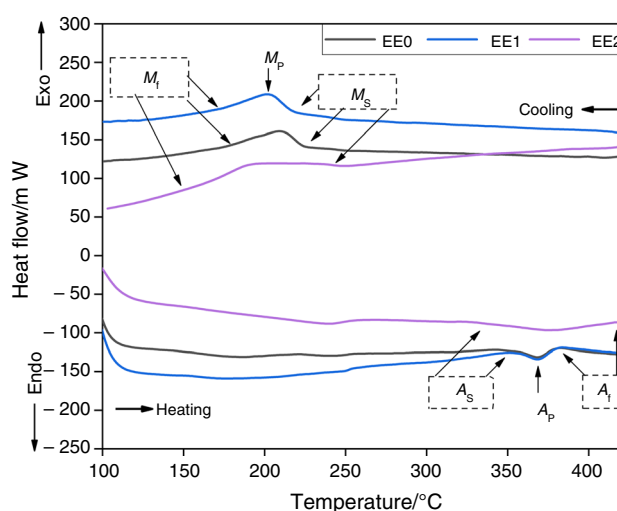

Fig. 4 DSC curves of alloys

provided in Table 4, it is evident that the addition of Gd has an impact on the transformation temperatures of the alloys.

The hysteresis temperatures of smart materials play a crucial role in their repeated active operations [34]. In applications, where there are low or high temperature differences, it is desirable to have a narrow or wide hysteresis temperature band, respectively [35]. The alloy that has been produced in this study exhibits a wide hysteresis temperature range, making it suitable for applications with significant temperature variations. This characteristic enhances the versatility and potential applicability of the alloy in various industries and fields. The fact that the addition of Gd increases the hysteresis temperature of the CuAlTa alloy from 150 to 190 °C makes it more suitable for applications requiring a wide hysteresis temperature. However, it is important to investigate the factors such as dislocations, atomic radius,

Table 3 EDX results of regions determined in SEM images

Alloys	Location	Cu/mass%	Al/mass%	Ta/mass%	Gd/mass%
EE0	2H	83.00±0.6	16.20±0.6	0.80±0.7	–
	18R	82.79±0.6	16.27±0.6	0.94±0.8	–
	1 (β-Ta)	41.05±0.5	15.12±0.5	43.83±0.7	–
	2 (α(Cu))	85.22±0.6	13.79±0.5	0.99±0.5	–
	3 ($\alpha + \gamma_1'$)	82.23±0.5	16.04±0.3	1.73±0.4	–
EE1	2H	84.91±0.7	13.93±0.5	1.02±0.3	0.14±1.1
	18R	84.56±0.7	14.87±0.6	0.46±0.4	0.11±0.9
	1 (β-Ta)	30.38±0.6	8.65±0.5	60.63±0.6	0.34±0.7
	2 (snow crystal)	85.27±0.7	14.15±0.6	0.43±0.4	0.15±1.0
	3 ($\alpha + \gamma_1'$)	82.49±0.6	14.23±0.5	3.13±0.8	0.15±1.0
EE2	2H	84.89±0.6	14.40±0.6	0.55±0.6	0.16±0.6
	18R	82.07±0.6	16.01±0.5	1.78±0.5	0.14±0.8
	1 (β-Ta)	21.46±0.5	11.32±0.6	66.73±0.6	0.49±0.7
	2 (α(Cu))	95.09±0.7	4.20±0.6	0.58±0.7	0.13±0.9
	3 ($\alpha + \gamma_1'$)	81.85±0.5	16.81±0.5	1.18±0.6	0.16±0.8

Table 4 Transformation temperatures obtained by DSC analysis of alloys

Alloys	A_s/°C	A_p/°C	A_f/°C	M_s/°C	M_p/°C	M_f/°C	$H_t(A_f - M_s)$/°C
EE0	355.3	368.9	379.5	224.2	210.7	185.3	158.2
EE1	358.0	369.6	378.7	214.9	202.1	173.5	167.5
EE2	330.1	377.5	415.3	225.9	194.6	148.4	182.9

stress, precipitate, etc., that influence the change in hysteresis temperature [35]. The SEM images of the precipitate structures reveal that Gd enlarges the precipitate structures. The growth in the precipitate phase structures is also evident from the strengthening of the XRD peaks of the precipitate phases. As a consequence, the hysteresis temperatures of the alloy tend to increase.

Transformation temperatures are influenced by both chemical and non-chemical forces [36]. The chemical driving force arises from the disparity in Gibbs free energy between the austenite and martensite phases. Non-chemical forces, on the other hand, stem from the elastic energy involved in shape and volume changes during the transformation process, as well as the dissipation of energy during phase transitions [34]. To calculate these parameters, enthalpy ($\Delta H^{M \leftrightarrow A}$), the equilibrium temperature (T_0) and entropy ($\Delta S^{M \leftrightarrow A}$) values must be determined. The enthalpy energies are determined by analyzing the phase transformation peaks on the DSC curves of the alloys using DSC software. The equilibrium temperature, at which the Gibbs free energy is equal, is calculated using the formula ($T_0 = \frac{M_s + A_f}{2}$) [37]. The entropy energy is calculated with [11];

$$\Delta S^{M \leftrightarrow A} = \Delta H^{M \leftrightarrow A}/T_0 \tag{1}$$

The entropy and enthalpy values of the alloys are presented in Table 5. The addition of Gd contributes to the broadening of the martensite transformation peaks, leading to an increase in both enthalpy and entropy energies. This change is visually illustrated in Fig. 5.

The thermoelastic phase transformation in alloys is related to the state of equilibrium reached during reverse transformations between chemical and non-chemical forces [36]. The Gibbs free energy required to explain this relationship is calculated with [11];

$$\Delta G^{A \rightarrow M}(M_s) = -(T_0 - M_s)\Delta S^{M \rightarrow A} \tag{2}$$

and the elastic energy is calculated with [25];

$$G_e = (M_s - M_f)\Delta S^{M \rightarrow A} \tag{3}$$

The Gibbs free energies and elastic energies obtained are listed in Table 5. It is observed that the Gibbs free energy, which is the energy difference between the austenite and martensite phases, increases with the addition of Gd. Similarly, the elastic energy is also affected by these changes. The expansion of the precipitate phases due to the increased contribution of Gd leads to greater shape and volume changes during the transformation, resulting in an increase in the elastic energy value. The SEM image of the EE2 alloy provides clear evidence of the growth of precipitate phases, which contributes to the elevated stresses during the transformation. This observation aligns with the temperature and energy increases observed in the thermodynamic parameters, as depicted in Fig. 5. It is determined that the higher the entropy, the lower the order of the crystal structure [38]. Figure 6 illustrates the relationship between the quantities of Gibbs free energy, elastic energy, and entropy, allowing for a comparison among them. This comparison provides a clearer understanding of their interrelationship. Notably, in Fig. 6, it can be observed that the EE2 sample exhibits the most ordered crystal structure among the alloys.

The bend testing analysis, aimed at evaluating the shape memory behavior of the alloys, yielded the results summarized in Table 1. Additionally, the experimental images of the alloys after undergoing the bend test are presented in Fig. 7. The shape recovery rate (SRR) ratios for the EE0, EE1, and EE2 alloys were determined to be 56.14%, 56.66%, and 58.46%, respectively. Compared to previous studies [13], it is observed that the SRR ratio of the EE0 alloy, which is produced by increasing the concentrations of Cu and Al elements and decreasing the concentration of Ta, shows an increase. The SRR ratios of the EE1 and EE2 alloys, produced by reducing the Cu concentration and replacing it with Gd, show a slight increase. The increase in the SRR ratio, despite the higher precipitation phases in the

Table 5 Some calculated thermodynamic parameters of alloys

Alloys	T_0/°C	$\Delta G^{A \rightarrow M}$/J g^{-1}	G_e/J g^{-1}	$\Delta S^{A \rightarrow M}$/J g^{-1}°C^{-1}	$\Delta S^{M \rightarrow A}$/J g^{-1}°C^{-1}	$\Delta H^{M \rightarrow A}$/J g^{-1}	$\Delta H^{A \rightarrow M}$/J g^{-1}
EE0	301.8	1.08	1.46	3.7	14.0	4.23	1.41
EE1	296.8	0.74	1.04	2.5	9.0	2.69	0.75
EE2	320.6	1.75	8.24	10.6	18.5	5.95	3.41

Fig. 5 The obtained enthalpy
variations and entropy varia-
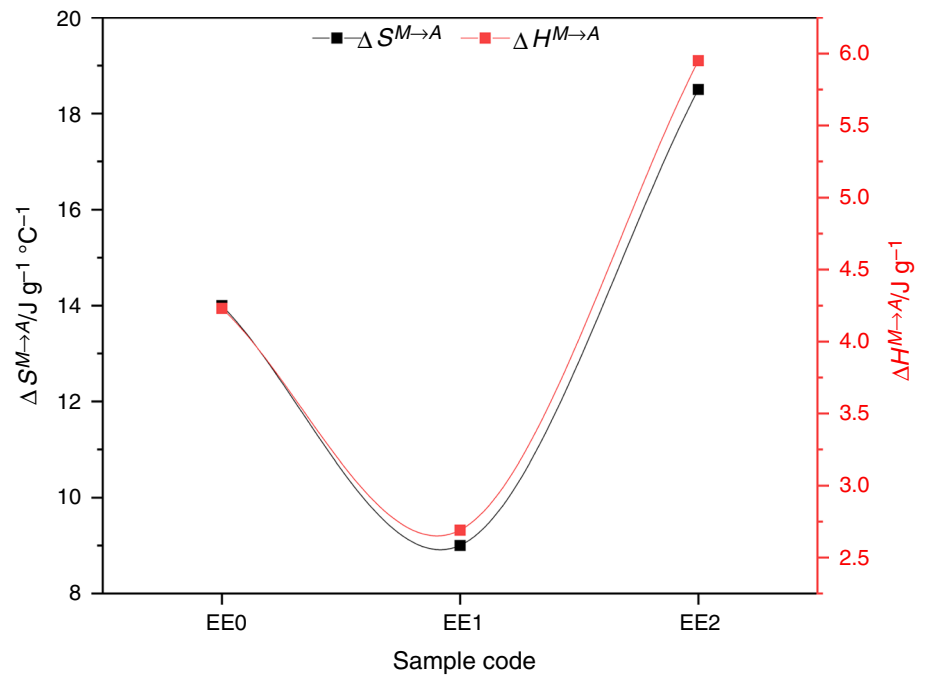tions of alloys

Fig. 6 Graphical representa-
tion of the relationship between
entropy, Gibbs free energy and
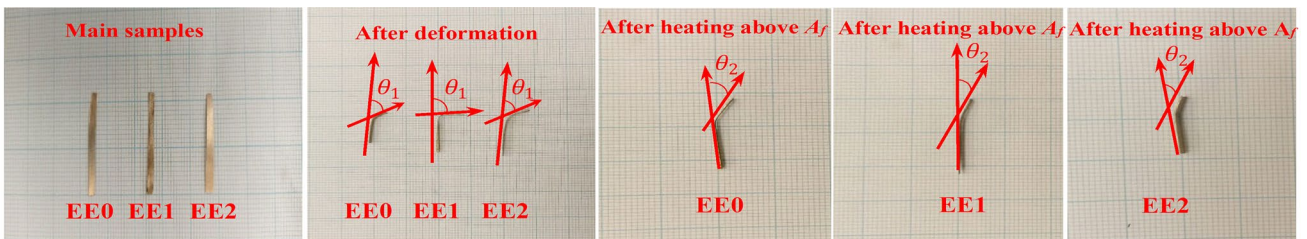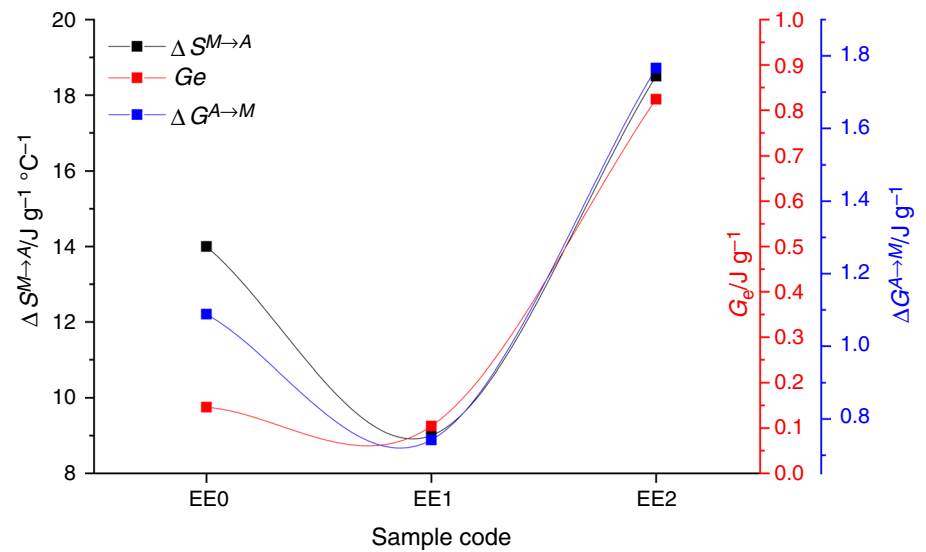elastic energy changes of alloys

Fig. 7 Positions of alloys before and after bend testing

EE1 and EE2 alloys, indicates that the Gd element improves the shape recovery behavior.

Grains are formed by the combination of several crystallites, which consist of unit cells. The diffraction pattern is known to be related to the full width at half height (FWHM) using Scherrer's equation [39]. The XRD data obtained for the crystalline size is closely matched to the reference code in the X'pert High Score software, and the FWHM is calculated for each diffraction peak. B represents FWHM in radians; $K = 2[\ln(2)/\pi]1/2$ is Scherrer's constant and is of the order of $\cong 0.9$; λ is the X-ray wavelength, d is the average size of the crystalline, and θ is the Bragg angle in degrees [40, 41].

$$\text{Crystallite size } (d) = K\lambda/B\cos\theta \tag{4}$$

The presence of phase structures, combined with multiple crystallites composed of unit cells, signifies a relationship between grain size, crystallite size, and phase structures. This relationship leads to an impact on the martensite transformation due to the influence of existing martensite phase structures on crystallite size. Consequently, the microstructure of the alloy, including grain size, phases, defects, and martensitic types and variants, undergoes changes depending on the alloy's composition and the manufacturing and processing techniques employed [42]. Numerous studies have reported that changes in crystallite size impact mechanical performance [43–45]. In the CuAlNi system alloy, the addition of Ti elements resulted in inhibited precipitate phases and reduced crystallite size [45]. Similarly, the introduction of Ag element to the CuAlNi alloy led to decreased crystallite sizes and influenced phase transformation temperatures, serving as a primary control factor [44].

Narasimha et al. [46] reported a reduction in crystallite size by 89% in the CuAlBe alloy with the addition of Zr. In the CuAlTa alloy, the addition of 0.5% (w.t) Gd increased the crystallite size from 32.02 to 51.64 nm. However, with an increase in Gd ratio to 1%, the crystallite size decreased to 39.86 nm. The calculation of crystallite size takes into account both the dominant phases and their densities. SEM images at the same magnifications reveal that in the EE1 alloy with 0.5% (w.t) Gd, all phase structures appear larger, whereas in the EE2 alloy with 1% (w.t) Gd, the phase structures become thinner and smaller. Notably, $\alpha(Cu)$ (2) phase structures exhibit coarser structures. However, the higher ratio of 18R, 2H, β-Ta and $\alpha + \gamma 1'$ phases than $\alpha(Cu)$ precipitate phases showed that 18R, 2H, β-Ta and $\alpha + \gamma 1'$ phases were more effective in calculating the crystallite size. The comparison between the phase number determined by XRD analysis and the crystallite size in Fig. 8 indicates that the crystallite size decreases with an increasing phase number (diffraction), while it increases with a decreasing phase number.

The microhardness of the alloys was measured at room temperature by averaging values obtained from five different regions, namely 18R, 2H, 1, 2, and 3. The microhardness value of the non-Gd additive EE0 alloy was measured as $271.9HV_{0.3}$ In contrast, the microhardness values for the Gd-added EE1 and EE2 alloys were measured as 283.8 and $260.7HV_{0.3}$, respectively. The microhardness values obtained in our study are consistent with the microhardness values reported by Ercan et al. for Cu-Al-Ta alloys, which

Fig. 8 The variation of the phase number determined by the XRD patterns with respect to grain size of alloys
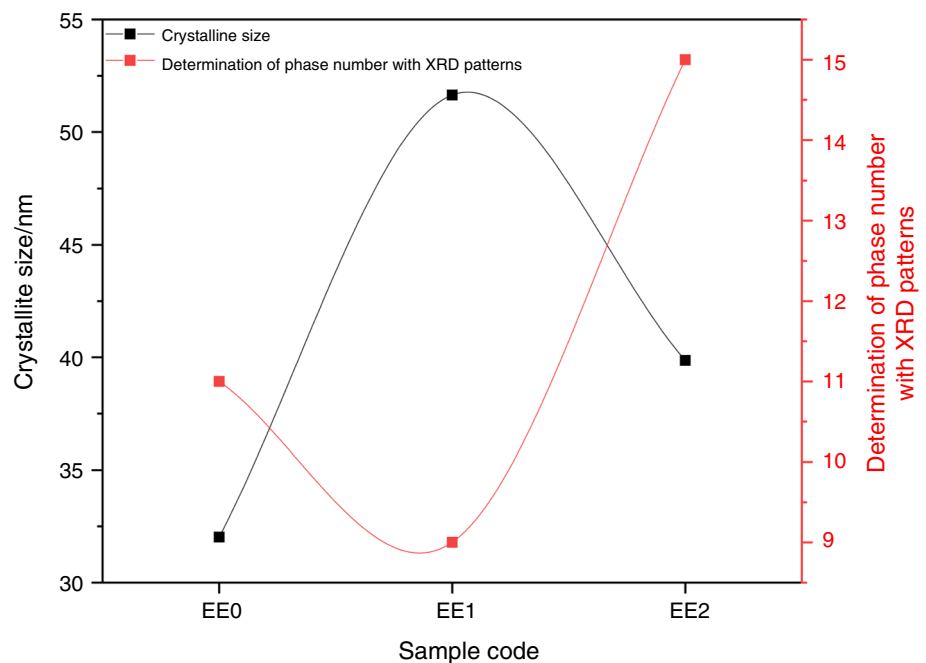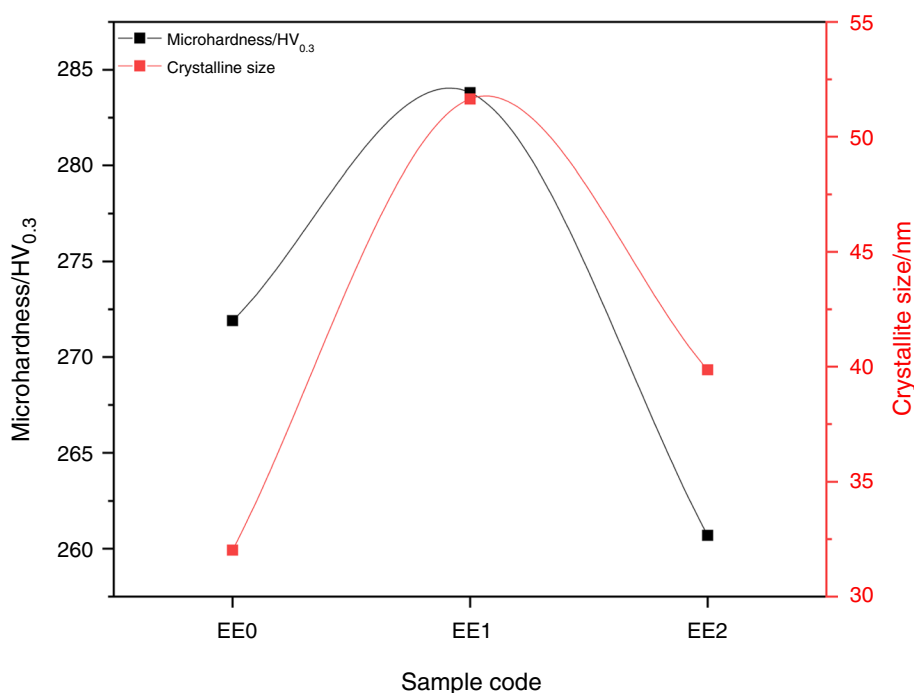
Fig. 9 The variation of micro-hardness with respect to grain size of alloys

range from approximately 200 HV to 290 HV [7]. In the EE0 and EE2 alloys, the microhardness values measured in the α(Cu) precipitate phase were 273.1 and 275.6 $HV_{0.3}$, respectively. In the EE1 alloy, which exhibited a snow crystal phase structure instead of the α(Cu) precipitate phase, the microhardness was measured as 294.9 $HV_{0.3}$. A similar study also reported an increase in microhardness due to the high volume fraction of the snow crystal structure [47, 48]. Another factor contributing to the increased microhardness is the higher volume fraction of β-Ta phase structures in the EE1 alloy compared to the EE0 and EE2 alloys. The broadening of XRD peaks (FWHM) is attributed to an increase in the density of crystal defects, including voids, dislocations, and stacking errors, as well as the strengthening of precipitate structures and the growth of internal strains [49]. Figure 9 illustrates the impact of crystallite sizes on microhardness values, showing a linear relationship between microhardness and crystallite sizes.

Conclusions

The results obtained from various analyses, including optical microscopy, SEM–EDX, microhardness, XRD, DSC, and bend testing, for the EE0, EE1, and EE2 alloys, which were produced by varying the ratios of Cu and Gd elements while keeping the Al and Ta element ratios constant, are summarized as follows:

- Based on the XRD results, it was identified that the main phases present in the alloys were martensite β_1' (18R) and austenite γ_1' (2H). Additionally, the alloys exhibited the presence of Al_3Ta (DO19) and α(Cu) phases. The inclusion of Gd element resulted in the formation of the intermetallic phase structure Al_3GdCu_2 (DO19). Due to the rapid cooling process, the phase transitions involving β_1', γ_1', α(Cu) and Al_3Ta phases were not fully completed, leading to the coexistence of phase compounds such as $\beta_1' + \gamma_1'$, α(Cu) + γ_1', α(Cu) + β_1', α(Cu) + Al_3GdCu_2 and $Al_3Ta + Al_3GdCu_2$, which were intertwined with each other.

- Thin needle-like β_1' (18R) and thick plate-like γ_1' (2H) structures were clearly seen in SEM images and confirmed by optical microscope images. SEM images identified structures numbered 1, 2, and 3 as belonging to the β-Ta phase, the α(Cu) precipitate phase, and the $\alpha + \gamma_1'$ phase structure, respectively. In the EE0 alloy, there was an observed increase in the size of the pit-form α(Cu) phase structures. However, in the EE1 alloy, these α(Cu) phase structures exhibited a snow crystal-like form.

- The optical microscope images revealed that the martensite (β_1') and austenite (γ_1') phase structures, as determined by XRD and SEM–EDX analyses, were separated by grain boundaries, and small-sized α(Cu) precipitate phases were present.

- The DSC analysis results revealed that the inclusion of Gd did not have an impact on the high-temperature shape memory characteristic of the alloy. However, it did modify other thermodynamic parameters. The hysteresis

temperature was observed to rise with the addition of Gd, making the material suitable for applications that involve high-temperature operations. The entropy, Gibbs free energy, and elastic energy values indicated that the EE2 alloy, which had the highest Gd content, exhibited the most organized crystal structure.

- It was observed that the addition of Gd resulted in a decrease in the crystallite size, particularly in the martensite and austenite phase structures, compared to the precipitate phase structures. This alteration in the phase composition contributed to a slight enhancement in the SRR rate.
- The EE1 alloy exhibited the highest microhardness value among the alloys studied, which can be attributed to the significant volume fraction of snow crystal-like and β-Ta phase structures present in this alloy.

Data availability The data associated with a paper are available, and under what conditions the data can be accessed.

Code availability Not applicable.

Declarations

Conflict of interest The authors state that there is no conflict of interest in the printing of this manuscript.

References

1. Otsuka K, Ren X. Recent developments in the research of shape memory alloys. Intermetallics. 1999;7(5):511–28.
2. Jani JM, Leary M, Subic A, Gibson MA. A review of shape memory alloy research, applications and opportunities. Mater Design 1980–2015. 2015;19(56):1078–113.
3. Tadaki T, Otsuka K, Shimizu K. Shape memory alloys. Annu Rev Mater Sci. 1988;18(1):25–45.
4. Kajiwara S. Characteristic features of shape memory effect and related transformation behavior in Fe-based alloys. Mater Sci Eng A. 1999;273:67–88.
5. Van Humbeeck J. Shape memory alloys: a material and a technology. Adv Eng Mater. 2001;3(11):837–50.
6. Fang C, Wang W, Fang C, Wang W. Introduction to shape-memory alloys. Shape memory alloys for seismic resilience. 2020.1–41.
7. Ercan E, Dagdelen F, Qader I. Effect of tantalum contents on transformation temperatures, thermal behaviors and microstructure of CuAlTa HTSMAs. J Therm Anal Calorim. 2020;139(1):29–36.
8. Balcı E, Dagdelen F. Thermal, structural properties and potential dynamic corrosion study of Ti-27Ni-21Nb-2Ta SMA. Iran J Sci Technol Trans A Sci. 2022;46(1):353–9.
9. Baram J, Rosen M. On the nature of the thermoelastic martensitic phase transformation in Au-47.5 at.% Cd determined by acoustic emission. Acta Metall. 1982;30(3):655–62.
10. Balci E, Dagdelen F. The comparison of TiNiNbTa and TiNiNbV SMAs in terms of corrosion behavior, microhardness, thermal and structural properties. J Therm Anal Calorim. 2022;147(20):10943–9.
11. Mohammed SS, Kok M, Qader IN, Kanca MS, Ercan E, Dağdelen F, et al. Influence of Ta additive into Cu 84–x Al 13 Ni 3 (wt%) shape memory alloy produced by induction melting. Iran J Sci Technol Trans A Sci. 2020;44:1167–75.
12. Dagdelen F, Aydogdu Y. Transformation behavior in NiTi–20Ta and NiTi–20Nb SMAs: transformation temperatures, microstructure and micro-hardness. J Therm Anal Calorim. 2019;136:637–42.
13. Ercan E. Effects of quenching temperatures on microstructure, phase transformation characteristics and shape memory behaviors of CuAlTa and CuAlTaNb HTSMAs. Trans Indian Inst Met. 2022;75(8):2041–50.
14. Degeratu S, Rotaru P, Rizescu S, Bîzdoacă N. Thermal study of a shape memory alloy (SMA) spring actuator designed to insure the motion of a barrier structure. J Therm Anal Calorim. 2013;111:1255–62.
15. Ma J, Karaman I, Noebe RD. High temperature shape memory alloys. Int Mater Rev. 2010;55(5):257–315.
16. Dagdelen F, Kanca M, Kok M. Effects of Different quenching treatments on thermal properties and microstructure in quaternary Cu-based HTSMA. Phys Met Metall. 2019;120:1378–83.
17. Yildiz K, Balci E, Akpinar S. Quenching media effects on martensitic transformation, thermodynamic and structural properties of Cu–Al–Fe–Ti high-temperature shape memory alloy. J Therm Anal Calorim. 2017;129:937–45.
18. Balci E, Dagdelen F, Mohammed SS, Ercan E. Corrosion behavior and thermal cycle stability of TiNiTa shape memory alloy. J Therm Anal Calorim. 2022;147(24):14953–60.
19. Narayana P, Kim S-W, Hong J-K, Reddy N, Yeom J-T. Estimation of transformation temperatures in Ti–Ni–Pd shape memory alloys. Met Mater Int. 2018;24:919–25.
20. Buenconsejo PJS, Kim HY, Hosoda H, Miyazaki S. Shape memory behavior of Ti–Ta and its potential as a high-temperature shape memory alloy. Acta Mater. 2009;57(4):1068–77.
21. Aydogdu Y, Turabi AS, Kok M, Aydogdu A, Tobe H, Karaca HE. Effects of the substitution of gallium with boron on the physical and mechanical properties of Ni–Mn–Ga shape memory alloys. Appl Phys A. 2014;117:2073–8.
22. Dasgupta R. A look into Cu-based shape memory alloys: present scenario and future prospects. J Mater Res. 2014;29(16):1681–98.
23. Mazzer E, da Silva M, Gargarella P. Revisiting Cu-based shape memory alloys: recent developments and new perspectives. J Mater Res. 2022;37(1):162–82.
24. Zhang X, Cui T, Liu Q, Dong Z, Man C. Effect of Nd addition on the microstructure, mechanical properties, shape memory effect and corrosion behaviour of Cu–Al–Ni high-temperature shape memory alloys. J Alloy Compd. 2021;858:157685.
25. Kwarciak J. Phase transformations in Cu-Al and Cu-Zn-Al alloys. J Therm Anal Calorim. 1986;31(3):559–66.
26. Velazquez D, Romero R. Spinodal decomposition and martensitic transformation in Cu–Al–Mn shape memory alloy. J Therm Anal Calorim. 2017;130(3):2007–13.
27. Kwarciak J, Bojarski Z, Morawiec H. Phase transformation in martensite of Cu-12.4% Al. J Mater Sci. 1986;21:788–92.

28. Zhang X, Sui J, Liu Q, Cai W. Effects of Gd addition on the microstructure, mechanical properties and shape memory effect of polycrystalline Cu-Al-Ni shape memory alloy. Mater Lett. 2016;180:223–7.

29. Oliveira A, Silva R. Thermomagnetic behavior of an as-quenched Cu-Al-Mn-Gd alloy. Mater Chem Phys. 2018;209:112–20.

30. Oliveira A, Paganotti A, Silva R. Kinetics of martensite decomposition in a Gd-modified Cu-Al alloy. J Phys Chem Solids. 2019;135:109074.

31. Adorno A, Silva R. Phase transformations in the Cu-Al alloy with Ag addition. J Therm Anal Calorim. 2005;79:445–9.

32. Sepulveda A, Muñoz R, Lovey F, Auguet C, Isalgue A, Torra V. Metastable effects on martensitic transformation in SMA: Part II. The grain growth effects in Cu-Al-Be alloy. J Therm Anal Calorim. 2007;89(1):101–7.

33. Wang C, Su Y, Yang S, Shi Z, Liu X. A new type of Cu–Al–Ta shape memory alloy with high martensitic transformation temperature. Smart Mater Struct. 2013;23(2):025018.

34. Liu Y. Some factors affecting the transformation hysteresis in shape memory alloys. Chen HR, editor. 2010.361–369.

35. Ortín J, Delaey L. Hysteresis in shape-memory alloys. Int J Non-Linear Mech. 2002;37(8):1275–81.

36. Chen H, Xu W, Luo Q, Li Q, Zhang Y, Wang J, et al. Thermodynamic prediction of martensitic transformation temperature in Fe-CX (X= Ni, Mn, Si, Cr) systems with dilatational coefficient model. J Mater Sci Technol. 2022;112:291–300.

37. Qader IN, Kok M, Cirak ZD. The effects of substituting Sn for Ni on the thermal and some other characteristics of NiTiSn shape memory alloys. J Therm Anal Calorim. 2021;145(2):279–88. https://doi.org/10.1007/s10973-020-09758-w.

38. Mohammed SS, Mediha K, Qader IN, Dağdelen F. The developments of piezoelectric materials and shape memory alloys in robotic actuator. Avrupa Bilim Teknol Derg. 2019;17:1014–30.

39. Fermin JR, Rincón CD, Castro JA. Microstructural analysis of AgIn 5 VI 8 (VI: S, Se, Te) ternary semiconductors by X-ray diffraction. Mater Res. 2019;22.

40. Monshi A, Foroughi MR, Monshi MR. Modified Scherrer equation to estimate more accurately nano-crystallite size using XRD. World J Nano Sci Eng. 2012;2(3):154–60.

41. Kök M, Al-Jaf AOA, Çirak ZD, Qader IN, Özen E. Effects of heat treatment temperatures on phase transformation, thermodynamical parameters, crystal microstructure, and electrical

42. resistivity of NiTiV shape memory alloy. J Therm Anal Calorim. 2020;139:3405–13.

42. Rabiei M, Palevicius A, Monshi A, Nasiri S, Vilkauskas A, Janusas G. Comparing methods for calculating nano crystal size of natural hydroxyapatite using X-ray diffraction. Nanomaterials. 2020;10(9):1627.

43. Khalil-Allafi J, Dlouhy A, Eggeler G. Ni4Ti3-precipitation during aging of NiTi shape memory alloys and its influence on martensitic phase transformations. Acta Mater. 2002;50(17):4255–74.

44. Saud SN, Hamzah E, Abubakar T, Bakhsheshi-Rad H, Farahany S, Abdolahi A, et al. Influence of Silver nanoparticles addition on the phase transformation, mechanical properties and corrosion behaviour of Cu–Al–Ni shape memory alloys. J Alloy Compd. 2014;612:471–8.

45. Saud SN, Hamzah E, Abubakar T, Zamri M, Tanemura M. Influence of Ti additions on the martensitic phase transformation and mechanical properties of Cu–Al–Ni shape memory alloys. J Therm Anal Calorim. 2014;118:111–22.

46. Narasimha GB, Murigendrappa S. Effect of zirconium on the properties of polycrystalline Cu-Al-Be shape memory alloy. Mater Sci Eng A. 2019;755:211–9.

47. Liu Y, Blandin J, Suery M, Kapelski G. Effect of cooling rate on the microstructure and microhardness of the CuZrAgAl alloy. Mater Charact. 2012;70:8–13.

48. Yang S, Su Y, Wang C, Liu X. Microstructure and properties of Cu–Al–Fe high-temperature shape memory alloys. Mater Sci Eng B. 2014;185:67–73.

49. Torabi A, Babaheydari R, Akbari G, Mirabootalebi S. Optimizing of micro-hardness of nanostructured Cu–Cr solid solution produced by mechanical alloying using ANN and genetic algorithm. SN Appl Sci. 2020;2:1–9.